aerospace

MDPI

Article

On the Aeroelasticity of a Cantilever Wing Equipped with the Spanwise Morphing Trailing Edge Concept

Jafar S. Pilakkadan [1], Rafic M. Ajaj [2,*], Zawar Haider [1] and Mohammadreza Amoozgar [3]

[1] Department of Aerospace Engineering, Khalifa University, Abu Dhabi P.O. Box 127788, United Arab Emirates; jafarsadiquempm@gmail.com (J.S.P.); 100057743@ku.ac.ae (Z.H.)
[2] Advanced Research and Innovation Center (ARIC), Department of Aerospace Engineering, Khalifa University, Abu Dhabi P.O. Box 127788, United Arab Emirates
[3] Faculty of Engineering, University of Nottingham, Nottingham NG7 2RD, UK
* Correspondence: rafic.ajaj@ku.ac.ae; Tel.: +97-12-3124-238

Abstract: This paper studies the aeroelastic behavior of a rectangular, cantilever wing equipped with the spanwise morphing trailing edge (SMTE) concept. The SMTE consists of multiple trailing edge flaps that allow controlling the spanwise camber distribution of a wing. The flaps are attached at the wing's trailing edge using torsional springs. The Rayleigh–Ritz method is used to develop the equations of motion of the wing-flap system. The use of shape functions allows for representing the wing as an equivalent 2D airfoil with generalized coordinates that are defined at the wingtip. Strip theory, based on Theodorsen's unsteady aerodynamic model, is used to compute the aerodynamic loads acting on the wing. A representative Padé approximation for Theodorsen's function is utilized to model the aerodynamic behaviors in a state-space form allowing time-domain simulation and analysis. The model is validated using a rectangular cantilever wing and the data are available in the literature. A comprehensive parametric comparison study is conducted to assess the impact of flap stiffness on the aeroelastic boundary. In addition, the potential of the SMTE to provide load alleviation and flutter suppression is assessed for a wide range of flight conditions, using a discrete (1-cosine) gust. Finally, the implementation and validation of a controller for a wing with SMTE for gust load alleviation are studied and controller parameters are tuned for a specific gust model.

Keywords: spanwise morphing trailing edge; aeroelasticity; gust load alleviation; controller

Citation: Pilakkadan, J.S.; Ajaj, R.M.; Haider, Z.; Amoozgar, M. On the Aeroelasticity of a Cantilever Wing Equipped with the Spanwise Morphing Trailing Edge Concept. *Aerospace* **2023**, *10*, 809. https://doi.org/10.3390/aerospace10090809

Academic Editors: Zhiping Qiu, Weixing Yuan and Mojtaba Kheiri

Received: 1 June 2023
Revised: 6 September 2023
Accepted: 8 September 2023
Published: 15 September 2023

1. Introduction

In recent years, extensive research has been carried out to develop gust load alleviation (GLA) systems. The aerodynamic forces generated by GLA systems modify the overall forces in such a way as to alleviate the structural turbulence response. Moreover, minimizing the impact of gusts by deploying an active GLA system, typically through the use of conventional control surfaces, is an integral part of modern aircraft design [1]. Bernhammer et al. [2] presented an experimental aeroservoelastic investigation of a novel load alleviation concept using trailing edge flaps. In their model, the flaps were free-floating and mass underbalanced, such that they may become unstable at operational velocities unless suppressed by their control system (trailing edge tabs). They found that limit cycle oscillation could be reached either through structural limiters or by control actions of the trailing edge tabs. In the latter case, the amplitude of the limit cycle oscillation could be adjusted to the required energy output. An energy balance between harvested power and power consumption for actuators and sensing systems was made showing that the vibration energy of limit cycle oscillations could be used to keep the amplitude of the limit cycle constant, while the electric batteries, powering up the load alleviation system, were being charged. Wildschek et al. [3] investigated the gust load response of a large 750-passenger Blended Wing Body (BWB) airliner for the identification of sizing cases for the aircraft structure. They designed a GLA system and evaluated it by numerical simulations to allow for structural weight saving. They concluded that the structural weight saving was mainly limited by the allowed load factors considered in such optimization, the finite control authority of the actuators, and the achievable reliability of the GLA system itself. Huvelin et al. [4] conducted a numerical simulation for the gust response along with experimental results at ONERA to present a gust load alleviation study. Numerical comparisons were performed using various techniques of gust modeling and finally, an application example for gust load alleviation was presented. Bekemeyer et al. [5] investigated the gust load alleviation for an airfoil and a large aircraft configuration using computational fluid dynamics. The results of the study were then used in designing a simple gust controller aimed at negating gust-induced loads via deploying conventional control surfaces. Pusch [6] studied the effectiveness of using distributed flaps for wing gust load alleviation. It was concluded that it is possible to simplify the controller design and tuning and achieve the desired performance by using the proposed allocation method. Dias and Hubbard [7] presented a novel approach to tackle the gust load alleviation problem by controlling the shape of the lift distribution profile along the span. The unsteady aerodynamics of a finite wing featuring multiple trailing edge flaps were modeled using the unsteady vortex lattice method (UVLM), yielding a linear, time-variant, high-order-state-space model. By using an aerodynamic mode shape and associated eigenvalues, this distributed approach allows control of the loads at all the points. Pusch et al. [8] discussed the optimization of control surface layout for gust load alleviation by using a nonlinear model of a large-scale flexible aircraft with unsteady aerodynamics. Compared to a GLA, the system using the original aileron configuration exhibited a 9% performance improvement. Furthermore, a trade-off study was carried out which enabled a target-oriented balancing between individual load channels. The significance of aileron size and position on overall GLA performance was demonstrated, and consideration was proposed for the preliminary aircraft design process.

Recently, spanwise morphing trailing edge (SMTE) concepts have attracted a lot of interest due to their ability to alter the spanwise camber distribution. SMTE can be considered a morphing aircraft technology that allows altering the spanwise camber distribution for a variety of purposes including control authority, load alleviation, drag reduction, and flutter suppression. For more details on camber morphing and its applications, the reader is advised to check Barbarino et al. [9] and Ajaj et al. [10]. Several studies have assessed the performance benefits of SMTE. For instance, Pankonien and Inman [11,12] proposed a modular SMTE concept that locally varied the trailing edge camber of a wing functioning as a modular replacement for conventional control surfaces without altering the spar box. Utilizing alternating active sections of Macro Fiber Composites (MFCs) driving internal compliant mechanisms and inactive sections of elastomeric honeycombs, the SMTE concept eliminated geometric discontinuities associated with shape change; increasing aerodynamic performance. The modular morphing wing is shown in Figure 1. Force and deformation analysis of a morphing wing was performed with a smooth surface and independent spanwise-varying control surface. Wind tunnel tests at a flow speed of 10 m/s were also carried out using a hardware demonstrator. Results indicated that the developed spanwise morphing trailing edge led to excellent aerodynamic and structural performance.

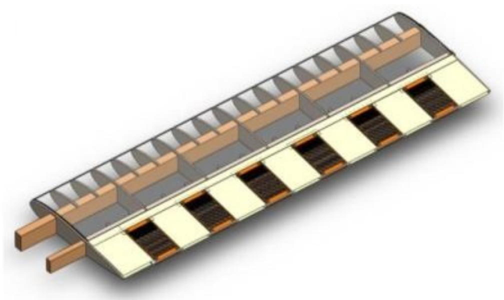

Figure 1. A finite wing with the SMTE concept [12].

Some recent analytical and experimental studies show the potential and feasibility of an active aeroelastic control system. The control surfaces are operated according to a control law that relates the motion of the controls to some measurements taken on the aircraft. Haghighat et al. [13] investigated the design optimization of an active load alleviation control system which was integrated with the design optimization of the aerodynamic shape and structural sizing of a UAV. Khalil and Fezans [1] discussed a methodology for designing combined feedback/feedforward GLA systems. The methodology applied to large aircraft and the simulation results showed the effectiveness of achieving the desired objectives while ensuring both design flexibility and control robustness and optimality. Capello et al. [14] discussed a comprehensive robust adaptive controller for gust load alleviation. They implemented and validated the proposed approach on subsonic aircraft for different mass flight conditions. Magar et al. [15] explored the use of origami to achieve camber morphing for vibration suppression and gust load alleviation of a typical wing section. Bourchak et al. [16] presented an optimum design of a PID controller for the adaptive torsion wing (ATW) using a genetic algorithm optimizer. In many papers, see (Kuznetsov et al. [17], Mozaffari-Jovin et al. [18], Vindigni et al. [19] and Munoz et al. [20]), various active wing-flutter suppression and control methods have been investigated. A morphing aircraft is usually associated with significant changes in the aerodynamic loads, structural/elastic properties, inertial properties, aeroelastic behavior, and flight dynamics and stability characteristics. This necessitates effective and robust control strategies to ensure certain stability and performance criteria are met during the morphing process. In addition, wing-shape changes require effective controllers to provide suitable actuation under various flight conditions and mission profiles. In summary, morphing can lead to complex time-varying nonlinear dynamical models with internal and external uncertainties [21,22]. These uncertainties and time-varying characteristics demand sophisticated control systems to confirm the stability and performance of the morphing wings.

It should be noted that several studies investigated the aeroelasticity of an airfoil with a flap. For example, Irani et al. [23] investigated limit cycle oscillations as well as nonlinear aeroelastic analysis of three degrees of freedom (dof) aeroelastic airfoil motion with cubic restoring moments in the pitch degree of freedom. The majority of studies in the literature have focused on developing SMTE concepts and assessing their performance characteristics; however, very little has been done on studying the aeroelasticity of SMTE [11,12]. SMTE concepts can have significant effects on the aeroelastic boundaries (divergence and flutter) and can be actively used to suppress some of the critical aeroelastic phenomena. This paper aims to fill this gap and conduct a comprehensive study on the aeroelasticity of SMTE. To achieve this, a rectangular, cantilever wing is equipped with an SMTE concept (consisting of three flaps). It is common for design studies to begin with low to medium-fidelity tools and move to higher-fidelity tools at later stages [24]. A low-fidelity aeroelastic model is developed using the Rayleigh–Ritz method coupled with strip theory aerodynamics. A parametric study is conducted to assess the impact of flap stiffness on the aeroelastic boundaries of the wing. Then, the ability of the SMTE to provide load alleviation is assessed and studied. Furthermore, a GLA controller is designed for SMTE and its effectiveness is assessed.

2. Aeroelastic Modeling

To simplify the analysis, a rectangular, cantilever wing equipped with three discrete flaps attached at the trailing edge is considered. Each flap is a rectangular segment connected to the wing using a torsional spring and the mechanical and geometric properties of each flap are uniform but might differ from one flap to another. The properties associated with each flap segment are listed in Table 1. The Rayleigh–Ritz method is used to develop the equation of motion for the wing with SMTE. The shape functions used here correspond to the uncoupled first bending and first torsion modes of a uniform cantilever beam. In addition, a shape function for each flap is used. This allows the wing with SMTE to be modeled as an equivalent airfoil with generalized coordinates that are defined at the wingtip.

Figures 2 and 3 show the layout of the wing with SMTE and the corresponding nomenclature used. Using standard notation, the mass of wing-flap per unit span is denoted by m, the plunging deflection is denoted by h, positive in the upward direction; α is the pitch angle about the elastic axis, positive when nose-up; and β_i is the control surface angle of i^{th} flap, positive when the trailing edge (TE) flap is moved down. The elastic axis is located at a distance ab from the mid-chord, where b is semi-chord, while the wing mass center is located at a distance $x_\alpha b$ from the elastic axis. The axis of rotation for the i^{th} control surface is located at a distance c_i from the mid-chord for the i^{th} wing segment, while the center of mass of the i^{th} flap is located at a distance x_{β_i} from the hinge. All distances are positive when measured towards the TE of the airfoil. In Figure 2, K_h, K_α and K_{β_i} are the stiffness in plunge, pitch, and the i^{th} flap, respectively.

Table 1. Geometric and Mechanical Properties of the Multi-flap Wing.

Parameter	Flap 1	Flap 2	Flap 3
Torsional stiffness	$K_{\beta 1}$	$K_{\beta 2}$	$K_{\beta 3}$
Length	l_1	l_2	l_3
Mass per unit span	m_{f1}	m_{f2}	m_{f3}
Mass moment of inertia per unit span	$I_{\beta 1}$	$I_{\beta 2}$	$I_{\beta 3}$
Static moments	$S_{\beta 1}$	$S_{\beta 2}$	$S_{\beta 3}$
Distance of flap mass center from c	$x_{\beta 1}$	$x_{\beta 2}$	$x_{\beta 3}$
Spanwise position	$0 \leq y \leq l_1$	$l_1 \leq y \leq l_2 + l_1$	$l_1 + l_2 < y \leq l_1 + l_2 + l_3$

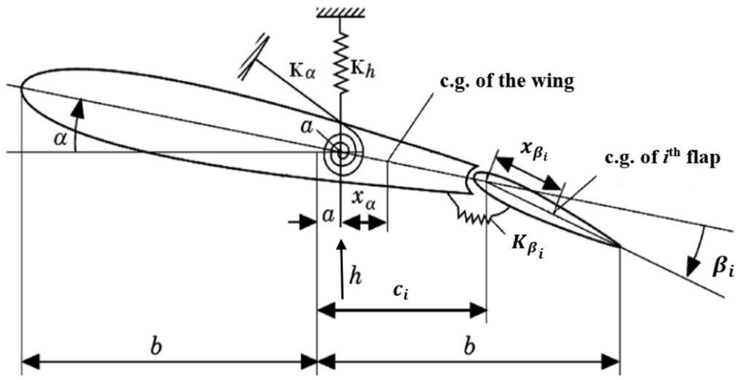

Figure 2. Schematic of an airfoil section with a control surface.

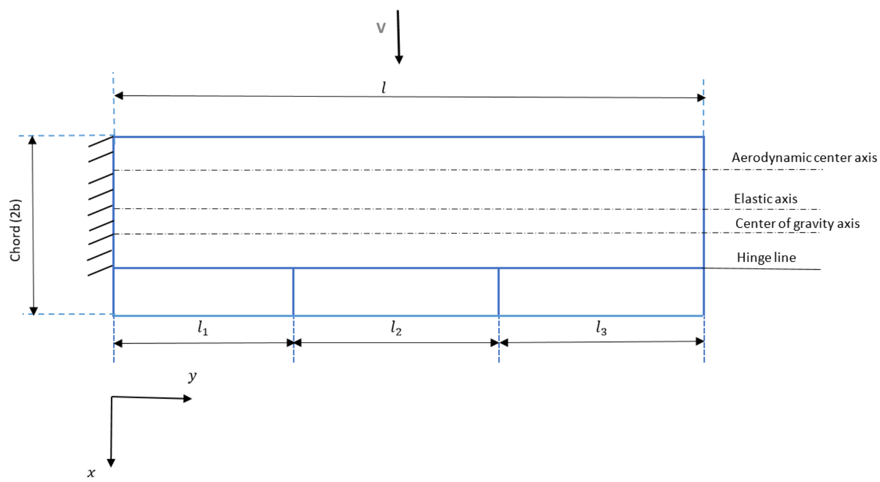

Figure 3. A top view of the SMTE.

The continuous, multi-degree of freedom, wing structure is modeled as two degrees of freedom system via the Rayleigh–Ritz method using shape functions. These shape functions correspond to the uncoupled first bending and first torsional modes of a uniform cantilever beam. The first bending shape function, $f(y)$, is given as:

$$f(y) = 0.5[(\cosh(B_n y) - \cos(B_n y)) - \sigma_n(\sinh(B_n y) - \sin(B_n y)] \tag{1}$$

where y is the spanwise position measured from the wing root and

$$\sigma_n = \frac{(\cosh(B_n l) + \cos(B_n l))}{(\sinh(B_n l) + \sin(B_n l))} \tag{2}$$

where l is the wing semi-span and

$$B_n l = 1.875 \tag{3}$$

the torsion shape function, $\phi(y)$, is given as

$$\phi(y) = \sin\left(\frac{\pi}{2l} y\right) \tag{4}$$

Similarly, to obtain the torsion shape functions of the flap and its boundary is given as,

$$\Psi_i(y) = 1, \begin{cases} \Psi_1(y) = 1, \Psi_2(y) = 0, \Psi_3(y) = 0 & 0 \le y \le l_1 \\ \Psi_1(y) = 0, \Psi_2(y) = 1, \Psi_3(y) = 0 & l_1 < y \le l_1 + l_2 \\ \Psi_1(y) = 0, \Psi_2(y) = 0, \Psi_3(y) = 1 & l_1 + l_2 < y \le l_1 + l_2 + l_3 \end{cases} \tag{5}$$

Using the variable separation approach and shape functions, the plunge displacement, speed, and acceleration at any spanwise location (y) can be related to those of the wingtip (generalized coordinates) as:

$$\begin{aligned} h(t,y) &= h_t(t) f(y) \\ \dot{h}(t,y) &= \dot{h}_t(t) f(y) \\ \ddot{h}(t,y) &= \ddot{h}_t(t) f(y) \end{aligned} \tag{6}$$

The pitch displacement, speed, and acceleration at any spanwise location (y) and time instant can now be related to those of the wingtip (generalized coordinates) as:

$$\begin{aligned} \alpha(t,y) &= \alpha_t(t)\phi(y) \\ \dot{\alpha}(t,y) &= \dot{\alpha}_t(t)\phi(y) \\ \ddot{\alpha}(t,y) &= \ddot{\alpha}_t(t)\phi(y) \end{aligned} \tag{7}$$

Similarly, the flap displacement, speed, and acceleration at any spanwise location (y) and time instant can now be related to those of the wingtip (generalized coordinates) as:

$$\begin{aligned} \beta_i(t,y) &= \beta_{t_i}(t)\Psi_i(y) \\ \dot{\beta}_i(t,y) &= \dot{\beta}_{t_i}(t)\Psi_i(y) \\ \ddot{\beta}_i(t,y) &= \ddot{\beta}_{t_i}(t)\Psi_i(y) \end{aligned} \tag{8}$$

where $h_t(t)$, $\alpha_t(t)$, and $\beta_{t_i}(t)$ represent the generalized coordinates coinciding with the wingtip and subscript 'i' in Equation (3) represents the flap number.

2.1. Equations of Motion

The kinetic energy (T) and potential energy (U) of the system can be expressed as:

$$\begin{aligned} T = \tfrac{1}{2}\, m\dot{h}_t^{\,2} \int_0^l f^2 dy \quad & + \tfrac{1}{2}\, I_\alpha \dot{\alpha}_t^{\,2} \int_0^l \phi^2 dy - S_\alpha \dot{h}_t \dot{\alpha}_t \int_0^l f\phi dy \\ & + \sum_{i=1}^{n} \Big\{ \tfrac{1}{2} \left(I_{\beta_i} \dot{\beta}_{ti}^{\,2} \int_0^l {\Psi_i}^2 dy \right) - \left(S_{\beta_i} \dot{h}_t \dot{\beta}_{ti} \int_0^l f \Psi_i dy \right) \\ & + \left(\dot{\alpha}_t \dot{\beta}_{ti} \left(I_{\beta_i} + b(c_i - a) S_{\beta_i} \right) \int_0^l \phi \Psi_i dy \right) \Big\} \end{aligned} \tag{9}$$

$$U = \frac{1}{2} GJ{\alpha_t}^2 \int_0^l \left(\frac{d\varnothing}{dy} \right)^2 dy + \frac{1}{2} EI{h_t}^2 \int_0^l \left(\frac{d^2 f}{dy^2} \right)^2 dy + \sum_{i=1}^{n} \frac{1}{2} \left(K_{\beta_i} {\beta_{t_i}}^2 \right) \int_0^l {\Psi_i}^2 dy \tag{10}$$

where I_α, and I_{β_i} are the mass moment of inertia of the wing and flap per unit span of the wing, respectively, S_α is the static moments of the wing, S_{β_i} is the static moments of the flap, and n is the total number of flaps. The equations of motion of the system using Lagrangian mechanics can be obtained as:

$$\frac{d}{dt}\left(\frac{\partial (T-U)}{\partial \dot{h}_t} \right) - \frac{\partial (T-U)}{\partial h_t} = L \tag{11}$$

$$\frac{d}{dt}\left(\frac{\partial (T-U)}{\partial \dot{\alpha}_t} \right) - \frac{\partial (T-U)}{\partial \alpha_t} = M_\alpha \tag{12}$$

$$\frac{d}{dt}\left(\frac{\partial (T-U)}{\partial \dot{\beta}_{ti}} \right) - \frac{\partial (T-U)}{\partial \beta_{ti}} = M_{\beta i} \tag{13}$$

where L and M_α are the generalized lift and pitching moment of the wing, respectively, and $M_{\beta i}$ is the moment about flap hinge points for the i^{th} flap. They can be expressed as:

$$L = \int_0^l L' h(y) dy,\ M_\alpha = \int_0^l {M_\alpha}' \phi(y) dy \ \ and \ \ M_{\beta i} = \int_0^l {M_{\beta i}}' \Psi_i(y) dy \tag{14}$$

where L', ${M_\alpha}'$, and ${M_{\beta i}}'$ are the generalized lift, pitching moment, and moment about flap hinge points per unit length, respectively.

2.2. Aerodynamic Loads

To compute the unsteady aerodynamic loads, the strip theory, based on Theodorsen's unsteady aerodynamic model, is used. Theodorsen's unsteady aerodynamics model has a circulatory component to account for the effect of the wake on the airfoil and it contains the main damping and stiffness terms and a non-circulatory component to account for the acceleration of the fluid surrounding the airfoil [25]. L' is the unsteady lift per unit span of the wing, ${M_\alpha}'$ is the pitching moment around the elastic axis per unit span of the wing, and ${M_{\beta i}}'$ is the moment about flap segments hinge point of the i^{th} flap per unit span of the wing. The expressions for L', ${M_\alpha}'$, and ${M_{\beta i}}'$ are taken from NACA Report No.496 [25]. It should be noted that the expression of ${M_{\beta i}}'$ varies from one flap to another depending on the properties of the flap.

$$L' = \pi\rho b^2 \left(-\ddot{h} + v\dot{\alpha} - ab\ddot{\alpha} - \tfrac{vT_{4i}}{\pi} \dot{\beta}_i - \tfrac{bT_{1i}}{\pi} \ddot{\beta}_i \right) + 2\pi\rho v b C(k) \left(-\dot{h} + v\alpha + b\left(\tfrac{1}{2} - a \right) \dot{\alpha} + \tfrac{vT_{10i}}{\pi} \beta_i + \tfrac{bT_{11i}}{2\pi} \dot{\beta}_i \right) \tag{15}$$

$$\begin{aligned} {M_\alpha}' = \pi\rho b^2 (& -ab\ddot{h} + \left(a - \tfrac{1}{2} \right) bv\dot{\alpha} - b^2 \left(\tfrac{1}{8} + a^2 \right) \ddot{\alpha} - (T_{4i} + T_{10i})\beta_i - \left(T_{1i} - T_{8i} - (c-a)T_{4i} + \tfrac{1}{2} T_{11i} \right) \tfrac{vb}{\pi} \dot{\beta}_i \\ & + (T_{7i} + (c-a)T_{1i}) \tfrac{b^2}{\pi} \ddot{\beta}_i \Big) \\ & + 2\pi\rho v b^2 \left(a + \tfrac{1}{2} \right) C(k) \left(-\dot{h} + v\alpha + b\left(\tfrac{1}{2} - a \right) \dot{\alpha} + \tfrac{vT_{10i}}{\pi} \beta_i + \tfrac{bT_{11i}}{2\pi} \ddot{\beta}_i \right) \end{aligned} \tag{16}$$

$$M_{\beta_i}{}' = \pi\rho b^2\Big(-T_{1i}\tfrac{b}{\pi}\ddot{h} - \Big(-2T_{9i} - T_{1i} - T_{4i}\Big(a - \tfrac{1}{2}\Big)\Big)\tfrac{vb}{\pi}\dot{\alpha} - 2T_{13i}\tfrac{b^2}{\pi}\ddot{\alpha} - (T_{5i} - T_{4i}T_{10i})\big(\tfrac{v}{\pi}\big)^2\beta_i \\ +T_{4i}T_{11i}\tfrac{vb}{2\pi^2}\dot{\beta}_i + T_{3i}\Big(\tfrac{b}{\pi}\Big)^2\ddot{\beta}_i\Big) \\ -\rho v b^2 T_{12i}C(k)\left(-\dot{h} + v\alpha + b\Big(\tfrac{1}{2} - a\Big)\dot{\alpha} + \tfrac{vT_{10i}}{\pi}\beta_i + \tfrac{bT_{11i}}{2\pi}\dot{\beta}_i\right) \tag{17}$$

Theodorsen's unsteady aerodynamics model has a frequency-dependent term, Theodorsen's transfer function which accounts for attenuation of lift amplitude and phase lag in the lift response due to sinusoidal motion. In this paper, unsteady lift per unit span and pitching moments per unit span are expressed in the time domain. Therefore, a Padé approximation developed by Brunton and Rowley [26] for Theodorsen's transfer function is used. The approximate transfer function $C(s)$ in the Laplace domain becomes

$$C(s) \approx \frac{0.5177\hat{a}^2s^2 + 0.2752\hat{a}s + 0.01576}{\hat{a}^2s^2 + 0.3414\hat{a}s + 0.01582} \tag{18}$$

where

$$\hat{a} = \frac{c}{2V} \tag{19}$$

The equivalent lift force becomes,

$$L = \tfrac{0.0985}{\hat{a}}\dot{u} \quad + \tfrac{0.0076}{\hat{a}^2}u + 0.5177\hat{B}\dot{h}_t\int_0^l f^2dy - \hat{A}\ddot{h}_t\int_0^l f^2dy + 0.5177\hat{B}V\alpha_t\int_0^l f\phi dy \\ +\Big(\hat{A}V + 0.5177\hat{B}Vb\Big(\tfrac{1}{2} - a\Big)\Big)\dot{\alpha}_t\int_0^l f\phi dy - \hat{A}ab\ddot{\alpha}_t\int_0^l f\phi dy + \Big(\beta_{ti}\int_0^l \tfrac{0.5177\hat{B}V}{\pi}\,T_{10i}f\Psi_i dy\Big) \\ +\Big(\dot{\beta}_{ti}\int_0^l\Big(\tfrac{0.5177\hat{B}b}{2\pi}T_{11i} - \tfrac{\hat{A}V}{\pi}T_{4i}\Big)f\Psi_i dy\Big) - \Big(\ddot{\beta}_{ti}\int_0^l \tfrac{\hat{A}b}{\pi}T_{1i}hf dy\Big) \tag{20}$$

and the pitching moment is given by

$$M_\alpha = \frac{0.0985}{\hat{a}}b\left(\frac{1}{2} + a\right)\dot{v} + \frac{0.0076}{\hat{a}^2}b\left(\frac{1}{2} + a\right)v - 0.5177\hat{B}b\left(\frac{1}{2} + a\right)\dot{h}_t\int_0^l f\phi dy - \hat{A}ba\ddot{h}_t\int_0^l f\phi dy \\ +0.5177b\left(\frac{1}{2} + a\right)\hat{B}V\alpha_t\int_0^l \phi^2dy - \left(b\left(a - \frac{1}{2}\right)\hat{A}V + 0.5177\hat{B}Vb^2\left(\frac{1}{2} + a\right)b\left(\frac{1}{2} - a\right)\right)\dot{\alpha}_t\int_0^l \phi^2dy \\ -\hat{A}b^2\left(\frac{1}{8} + a^2\right)\ddot{\alpha}_t\int_0^l \phi^2dy + \left(\beta_{ti}\int_0^l\left(\frac{0.5177b\left(\frac{1}{2} + a\right)\hat{B}V}{\pi}T_{10i} - \frac{\hat{A}V^2}{\pi}(T_{4i} + T_{10i})\right)\phi\Psi_i dy\right) \\ +\left(\dot{\beta}_{ti}\int_0^l\left(\frac{0.5177\hat{B}b^2\left(\frac{1}{2} + a\right)}{2\pi}T_{11i} - \frac{\hat{A}Vb}{\pi}\left(T_{1i} - T_{8i} - (c - a)T_{4i} + \frac{T_{11i}}{2}\right)\right)\phi\Psi_i dy\right) \\ -\left(\ddot{\beta}_{ti}\int_0^l\frac{\hat{A}b^2}{\pi}(T_{7i} + (c - a)T_{1i})\phi\Psi_i dy\right) \tag{21}$$

Similarly, the moment on the flap is given by

$$M_{\beta i} = \tfrac{0.0985}{\hat{a}}b\Big(-\tfrac{T_{12i}}{2\pi}\Big)\dot{w}_i \quad + \tfrac{0.0076}{\hat{a}^2}b\Big(-\tfrac{T_{12i}}{2\pi}\Big)v - 0.5177\hat{B}b\dot{h}_t\int_0^l\Big(-\tfrac{T_{12i}}{2\pi}\Big)f\Psi_i dy - \tfrac{\hat{A}b\ddot{h}_t}{\pi}\int_0^l T_{1i}f\Psi_i dy \\ +0.5177b\hat{B}V\alpha_t\int_0^l\Big(-\tfrac{T_{12i}}{2\pi}\Big)\phi\Psi_i dy \\ +\dot{\alpha}_t\int_0^l\Big(0.5177\hat{B}Vb^2\Big(\tfrac{1}{2} - a\Big)\Big(-\tfrac{T_{12i}}{2\pi}\Big) - \tfrac{\hat{A}Vb}{\pi}\Big(2T_{9i} - T_{1i} + \Big(a - \tfrac{1}{2}\Big)T_{4i}\Big)\Big)\phi\Psi_i dy - \tfrac{2\hat{A}b^2}{\pi}\ddot{\alpha}_t\int_0^l T_{13i}\phi\Psi_i dy \\ +\left(\beta_{ti}\int_0^l\left(\frac{0.5177b\left(-\frac{T_{12i}}{2\pi}\right)\hat{B}V}{\pi}T_{10i} - \frac{\hat{A}V^2}{\pi^2}(T_{5i} - T_{4i}T_{10i})\right)\Psi_i{}^2dy\right) \\ +\left(\dot{\beta}_{ti}\int_0^l\left(\frac{0.5177\hat{B}b^2\left(-\frac{T_{12i}}{2\pi}\right)}{2\pi}T_{11i} - \frac{\hat{A}Vb}{2\pi^2}(T_{4i}T_{11i})\right)\Psi_i{}^2dy\right) + \Big(\ddot{\beta}_{ti}\int_0^l\tfrac{\hat{A}b^2}{\pi^2}T_{3i}\Psi_i{}^2dy\Big) \tag{22}$$

$$\ddot{u} = \tfrac{-0.3414}{\hat{a}}\dot{u} - \tfrac{0.0158}{\hat{a}^2}u - \hat{B}\dot{h}_t\int_0^l f^2dy + \hat{B}V\alpha_t\int_0^l f\phi dy + \hat{B}b\Big(\tfrac{1}{2} - a\Big)\dot{\alpha}_t\int_0^l f\phi dy + \Big(\beta_{ti}\int_0^l\tfrac{\hat{B}V}{\pi}\,T_{10i}f\Psi_i dy\Big) + \Big(\dot{\beta}_{ti}\int_0^l\tfrac{\hat{B}b}{2\pi}T_{11i}f\Psi_i dy\Big) \tag{23}$$

$$\ddot{v} = \frac{-0.3414}{\hat{a}}\dot{v} - \frac{0.0158}{\hat{a}^2}v - \hat{B}\dot{h}_t\int_0^l f\phi dy + \hat{B}V\alpha_t\int_0^l \phi^2 dy + \hat{B}b\left(\frac{1}{2}-a\right)\dot{\alpha}_t\int_0^l \phi^2 dy + \left(\beta_{ti}\int_0^l \frac{\hat{B}V}{\pi}\, T_{10i}\phi\Psi_i dy\right) + \left(\dot{\beta_{ti}}\int_0^l \frac{\hat{B}b}{2\pi}T_{11i}\phi\Psi_i dy\right) \tag{24}$$

$$\ddot{w}_i = \frac{-0.3414}{\hat{a}}\dot{w}_i - \frac{0.0158}{\hat{a}^2}w_i - \hat{B}\dot{h}_t\int_0^l f\Psi_i dy + \hat{B}V\alpha_t\int_0^l \phi\Psi_i dy + \hat{B}b\left(\frac{1}{2}-a\right)\dot{\alpha}_t\int_0^l \phi\Psi_i dy + \left(\beta_{ti}\int_0^l \frac{\hat{B}V}{\pi}\, T_{10i}{\Psi_i}^2 dy\right) + \left(\dot{\beta_{ti}}\int_0^l \frac{\hat{B}b}{2\pi}T_{11i}{\Psi_i}^2 dy\right) \tag{25}$$

$$\hat{A} = \pi\rho b^2 \tag{26}$$

$$\hat{B} = 2\pi\rho V b \tag{27}$$

2.3. Aeroelastic Equations of Motion

The governing equation for aeroelastic analysis can be expressed as:

$$\mathrm{M}\ddot{\mathrm{X}} + \mathrm{D}\dot{\mathrm{X}} + \mathrm{KX} = F_a + F_g \tag{28}$$

where M, D, and K represent the structural mass, structural damping (set to zero here), and structural stiffness matrices of the wing-flap system, respectively; X represents the displacement vector in generalized coordinates and the elements of these matrices are represented in Appendix A; F_a represents the unsteady aerodynamic force vector; and F_g gust load vector and it is included only for the gust response and alleviation analysis.

2.4. The Gust Model

To evaluate the gust load alleviation capability of SMTE, it is essential to determine the variations in root bending moment and shear force (shown in Figure 4) when the wing encounters gusts. It is noted that here only the gust velocity based on a discrete, 1-cosine gust profile is considered. The 1-cosine gust profile is defined, according to FAR Part 25, Section 25.341, as:

$$w_g(\mathrm{t}) = \frac{\mathrm{U}_{ds}}{2}\left(1 - \cos\left(\frac{\pi V t}{H}\right)\right) \tag{29}$$

where H, the gust gradient, is the distance parallel to the airplane's flight path for the gust to reach its peak velocity, and it varies from 9.144 to 106.7 m. U_{ds} is the design gust velocity, and it can be expressed as:

$$\mathrm{U}_{ds} = \mathrm{U}_{ref}\mathrm{F}_g\left(\frac{H}{106}\right)^{\frac{1}{6}} \tag{30}$$

where U_{ref}, the reference gust velocity, has a magnitude of 17.07 m/s at sea level and reduces linearly from 17.07 to 13.4 m/s EAS at 15,000 feet. F_g is the flight profile alleviation factor, and it is set to one. The airspeed is set to 30 m/s and the angle of attack is kept at zero.

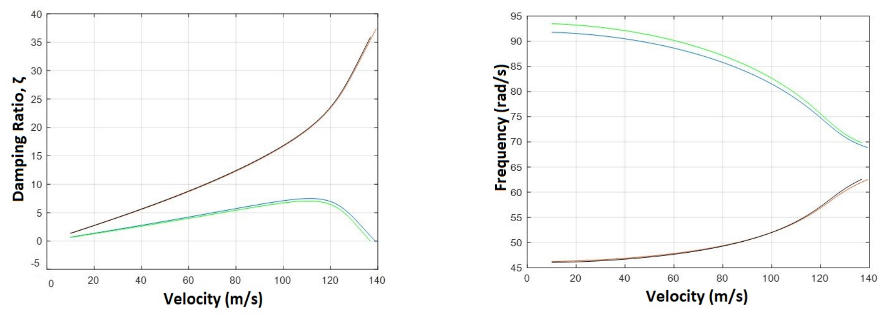

(**a**) Damping (**b**) Frequency

Figure 4. Flutter modes of Goland wing; blue for torsion and red for bending (with SMTE, K_β set to very high); green for torsion and black for bending (without SMTE).

2.5. Validation: Flutter Analysis

Due to the lack of available aeroelastic data on rectangular wings equipped with flap(s), the aeroelastic model developed here is validated using the Goland wing and the mechanical and geometric properties are listed in Table 2. For the sake of comparison, the stiffness of the three flaps is assumed to be very high (104 Nm/rad). This effectively limits the dynamics of the wing with SMTE to the bending-twisting of the cantilever wing. Figure 4 shows the variations in the first bending and the first torsion modes for the Goland wing with SMTE and the clean Goland wing (without SMTE). It can be seen that for the assumed high values of flap stiffness, the flutter mode for both scenarios is the 1st torsion mode. The flutter speed and frequency are 139.3 m/s and 68.87 rad/s for Goland with SMTE and 137.11 m/s and 69.9 rad/s for Goland without SMTE. This confirms the accuracy of the developed time-domain aeroelastic model. It should be noted that the flutter boundaries are estimated using the PK (frequency matching) method for validation purposes.

Table 2. Properties of Goland Wing [27].

Specifications	Goland Wing
Half span (m)	6.096
Chord (m)	1.8288
Mass per unit length (kg/m)	35.71
Moment of inertia (50% chord) (kgm)	8.64
Spanwise elastic axis (from LE)	33%
Center of gravity (from LE)	43%
Spanwise bending rigidity (Nm^2)	9.77×10^6
Torsional rigidity (Nm^2)	0.987×10^6
Density of air kg/m^3	1.225

3. Parametric Study

The Goland wing, equipped with the SMTE concept which consists of three flaps, is used here for parametric aeroelastic analysis. The purpose of this study is to identify the influence of various design parameters on the aeroelastic boundary. The loads due to gust are set to zero in this section.

Aeroelastic Boundaries: Flutter and Divergence

The flutter boundary of the cantilever wing with SMTE is obtained by calculating the critical flutter speed, flutter frequency, and divergence speed for different flap stiffness values. Figure 5a,b shows the variation in flutter speed and frequency for different flap stiffness of a cantilever wing with a single flap. Similarly, Figure 5c,d shows flutter speed and frequency for varying flap stiffness of SMTE (where the flap stiffnesses were changed simultaneously by the same amount).

Figure 5 shows that the wing with a single flap and the SMTE wing with three-flap configurations are similar in the variation in flap stiffness. It can be seen that the flutter speed is very sensitive to flap stiffnesses for a range between 10^3 and 10^5 Nm/rad. Further, an increase in stiffness from 10^5 Nm/rad does not affect flutter speed. The flutter frequency also shows the same trend as in the case of speed as after 10^5 Nm/rad stiffness, it remains constant. It should be noted that regardless of stiffness, the flutter mode does not change and it remains torsion mode for both wings. For flap stiffnesses above 10^5Nm/rad, the flutter speed for both configurations are increased from 90 m/s to 137 m/s and the frequency reduced from 85 rad/s to 69 rad/s. The flutter is determined to be due to the interaction of the first torsional and first bending mode, which excite each other and cause the torsional mode to become unstable. The low stiffness of the flap affects the globalized stiffness matrix and brings the first bending and first torsion frequencies closer to each other. This causes the coalescence of the modes to be brought about earlier in the presence of aerodynamic forces and causes the flutter to occur at a lower velocity.

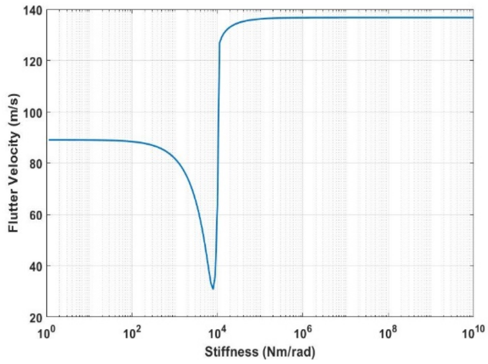

(**a**) Flutter Speed (Single Flap)

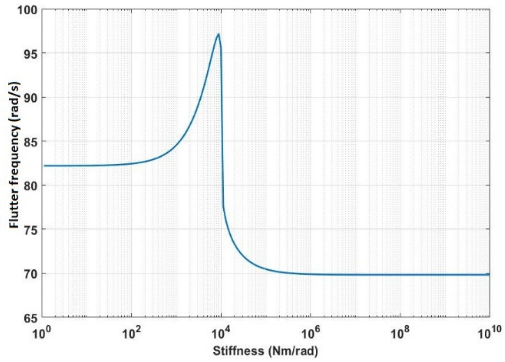

(**b**) Flutter Frequency (Single Flap)

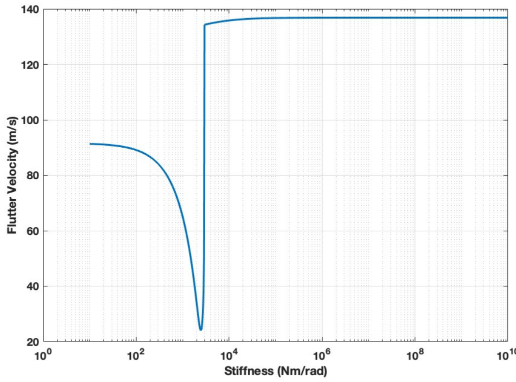

(**c**) Flutter Speed (SMTE)

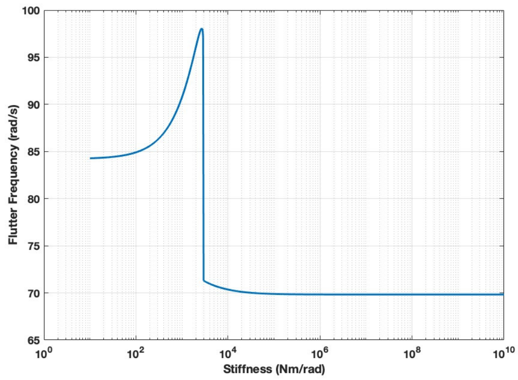

(**d**) Flutter Frequency (SMTE)

Figure 5. Variation in flutter speed and frequency with flap stiffness (**a**,**b**) for a single flap, and (**c**,**d**) for the SMTE wing.

Figure 6 shows the variation in flutter speed and frequency of a cantilever wing with SMTE (three-flap configuration) with the stiffness of each flap varied alone while keeping the other two stiffnesses at a value of baseline wing (10^8 Nm/rad). It can be seen that from Figure 6, the flutter boundary is not very sensitive to flap stiffnesses, but for a range between 10^3 and 10^5 Nm/rad shows a slight change and then it remains constant even when the stiffness increses further and the variations are identical in both velocity and frequency. It should also be noted that for flap stiffnesses above 10^5 Nm/rad, the flutter speed and frequency for the three-flap configuration are very similar to those for the single-flap configuration for all three configurations.

Figure 7 shows the variation in divergence speed for a range of flap stiffness varied from 10Nm/rad to 10^{10} Nm/rad. Four different configurations were considered; varying the stiffness of all three flaps of SMTE together (K_β; blue), for varying inboard flap stiffness ($K_{\beta 1}$; red) alone whilst keeping the other two stiffness at 10^8 Nm/rad, for varying midboard flap stiffness ($K_{\beta 2}$; yellow) alone whilst keeping the other two stiffness at 10^8 Nm/rad, and for varying outboard flap stiffness ($K_{\beta 3}$; magenta) alone whilst keeping the other two stiffness at 10^8 Nm/rad. The divergence behavior of the wing can be attributed to the presence of higher torsional loads being subjected to the structure in case of low flap stiffness. For a wing at low angle of attack and significantly low flap stiffness, the trailing edge of the flap will tend to move upwards, creating a negative lift force. Since this force is applied aft of the shear center, it will create nose-up torsional moments at the wing leading edge, and add to the possibility of divergence instability. It can be seen that from

Figure 7, the divergence boundary is different for all the four configurations for a range of flap stiffnesses (10 Nm/rad and 10^6 Nm/rad) and above 10^6 Nm/rad it become a single line having a divergence speed of 252.28 m/s which is same as goland wing [27]. The first configuration, K_β has the most deviated from the goland wing divergence speed and the inboard flap ($K_{\beta 1}$) is the least deviated from the goland wing divergence speed. It is evident from aeroelastic boundaries that the SMTE configuration is behaving very similarly to single flap configuration for stiffness values of above 10^6 Nm/rad, so in the following sections the analysis is carried out for stiffness value of 10^8 Nm/rad for all the flaps.

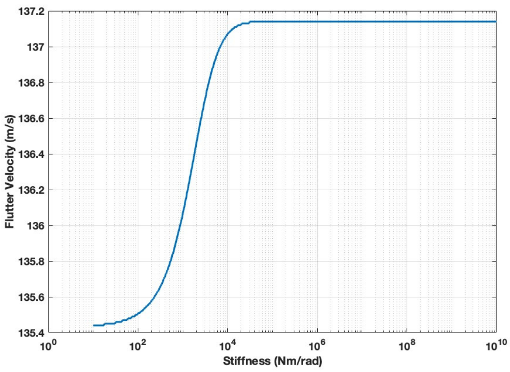

(**a**) Varying inboard flap stiffness ($K_{\beta 1}$)

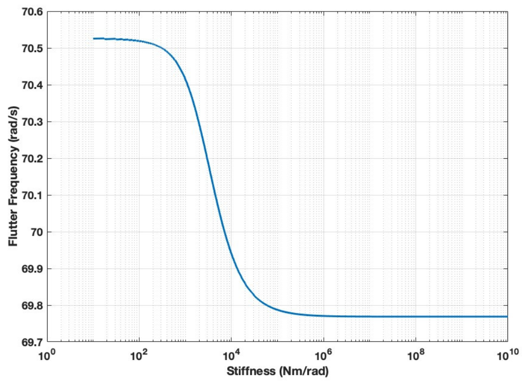

(**b**) Varying inboard flap stiffness ($K_{\beta 1}$)

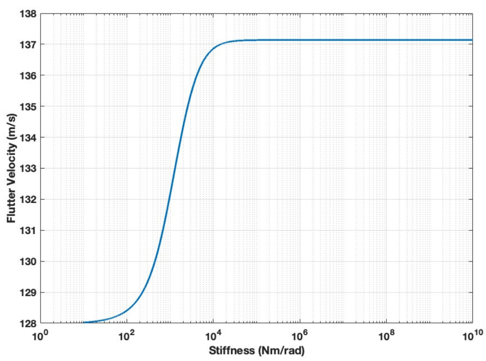

(**c**) Varying midboard flap stiffness ($K_{\beta 2}$)

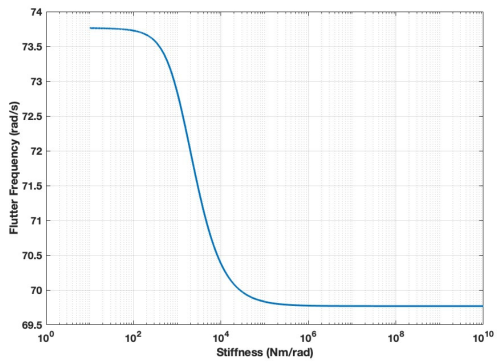

(**d**) Varying midboard flap stiffness ($K_{\beta 2}$)

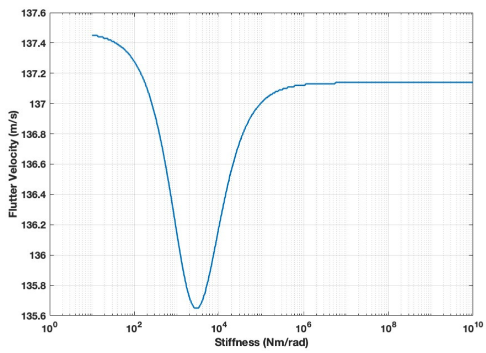

(**e**) Varying outboard flap stiffness ($K_{\beta 3}$)

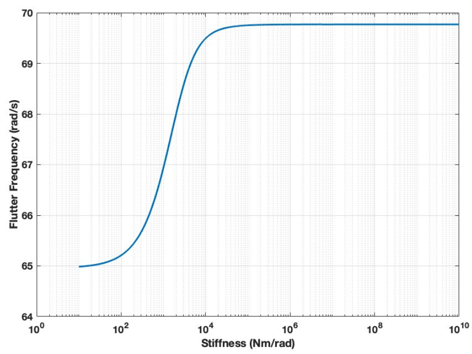

(**f**) Varying outboard flap stiffness ($K_{\beta 3}$)

Figure 6. Flutter speed and frequency of SMTE wing; (**a**,**b**) for varying inboard flap stiffness ($K_{\beta 1}$) alone; (**c**,**d**) for varying midboard flap stiffness ($K_{\beta 2}$) alone; (**e**,**f**) for varying outboard flap stiffness ($K_{\beta 3}$) alone.

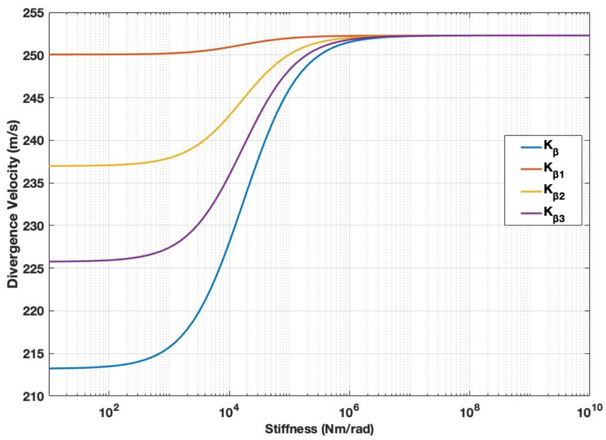

Figure 7. Divergence speed vs. stiffness of SMTE wing; for varying the stiffness of all flaps together (K_β); for varying inboard flap stiffness ($K_{\beta 1}$) alone; for varying midboard flap stiffness ($K_{\beta 2}$) alone; for varying outboard flap stiffness ($K_{\beta 3}$) alone.

4. Response to Discrete Gusts

The response of the wing with SMTE (three-flap configuration) is assessed for upward and downward, discrete gust with the minimum (H = 9.07 m) and maximum (H = 106.7 m) gust gradients. The airspeed is set to 30 m/s, the angle of attack is fixed to 0.2 radian, and the flap stiffnesses are set to 10^8 Nm/rad. In this paper, gust velocity based on a discrete, 1-cosine gust profile is considered and it is assumed that the flaps are deflected before the gust hits the wing and the loads are used where the gust velocity is assumed to result in an instantaneous change in angle of attack. Only the maximum load point is taken into consideration for each gust gradient. The dynamic analysis is out of the scope of this paper because the flaps are deflected before the gust hits the wing. This is based on an assumption that a LIDAR or a sensor is located at the nose of the aircraft to detect gust and based on the signal from the LIDAR/sensor, the wing will be already prepared in optimum shape when a gust arrives at it. To evaluate the load alleviation capability of SMTE, the root shear force (RSF) and root bending moment (RBM) variations for different flap angles are presented using carpet plots (Figures 8–11).

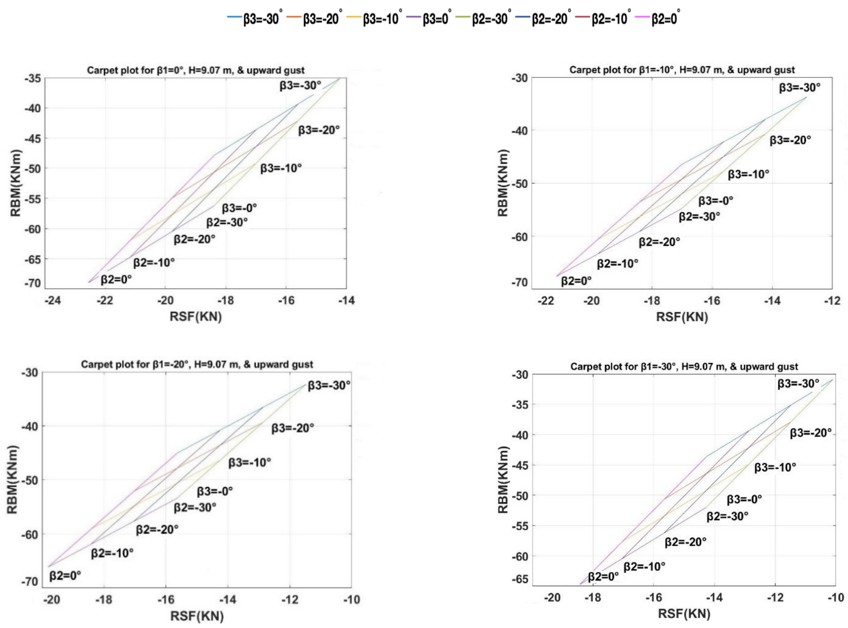

Figure 8. Carpet plot for upward gust for H = 9.07 m.

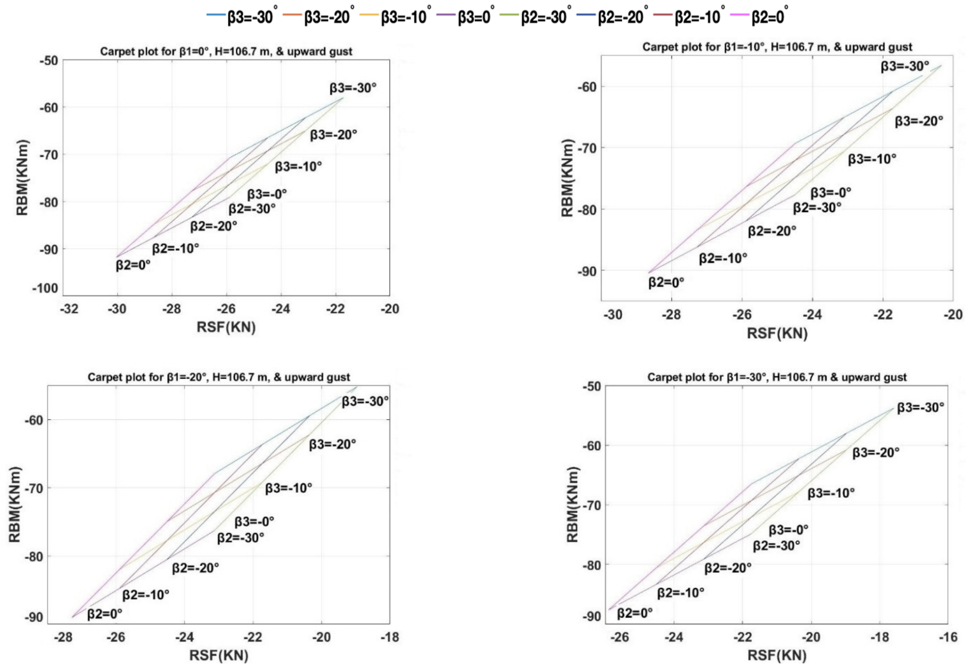

Figure 9. Carpet plot for upward gust for H = 106.7 m.

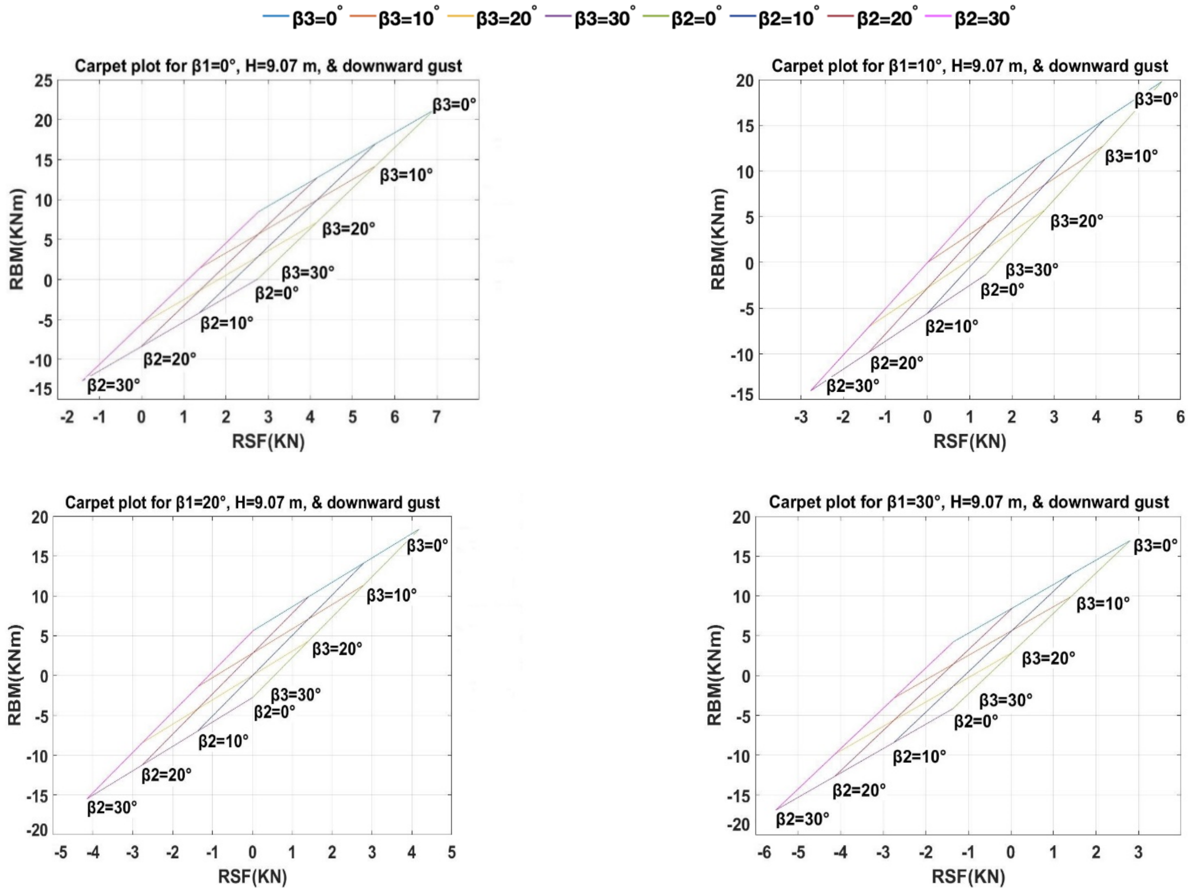

Figure 10. Carpet plot for downward gust for H = 9.07 m.

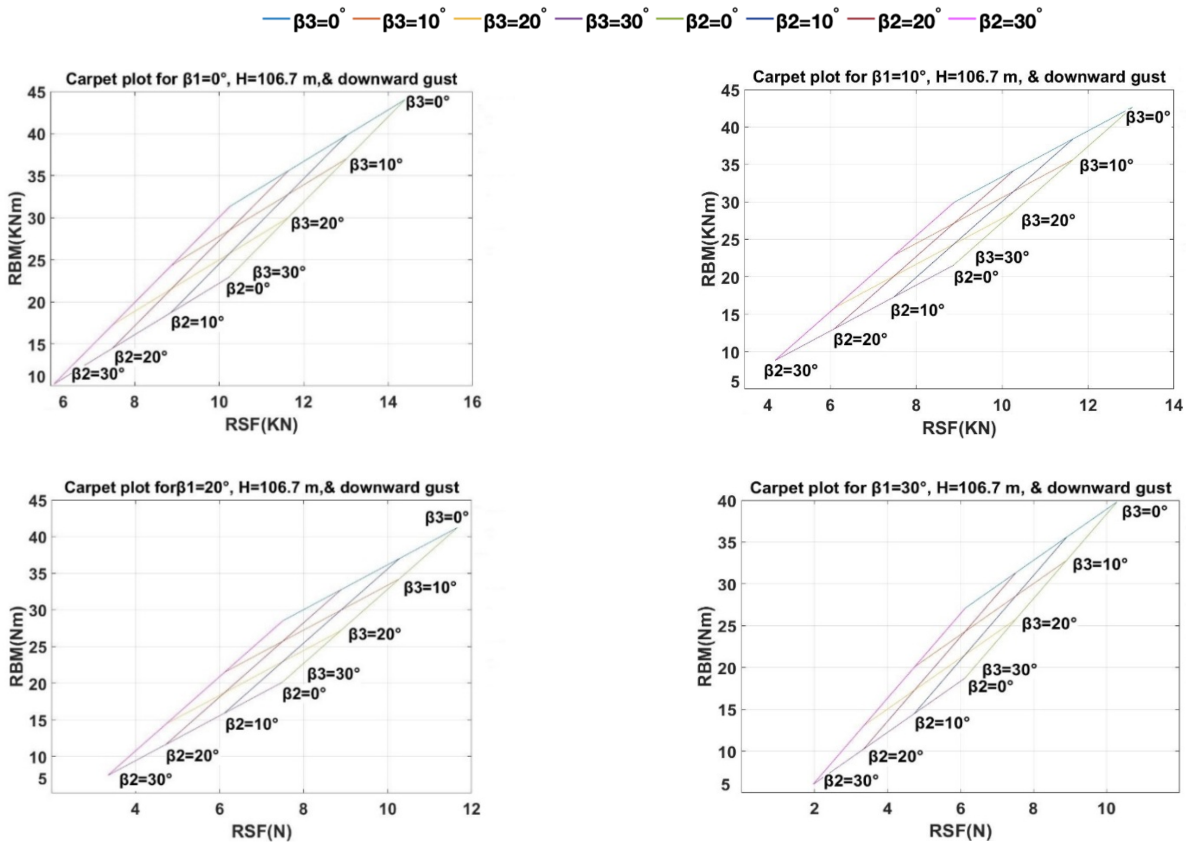

Figure 11. Carpet plot for downward gust for H = 106.7 m.

Upward-gust carpet plots are shown in Figures 8 and 9 and downward-gust carpet plots are shown in Figures 10 and 11. The carpet plots show an overview of the alleviation properties of SMTE for different combinations of flap deflections. For the upward gust, the upward flap deflections give alleviation in RSF and RBM while for the downward gust, the downward flap deflection gives alleviation in RSF and RBM. A more detailed gust load alleviation analysis and comparison with a single flap result are presented in the following sections.

4.1. Gust Load Alleviation Response Analysis

To identify the effectiveness of the location of different flaps in providing load alleviation capability of SMTE, each flap where deflected alone while keeping the other two flaps kept at zero flap angle in this subsection. Upward and downward gusts (1-cosine) are considered with an airspeed of 30 m/s, the angle of attack is fixed to 0.2 radian, the flap stiffnesses are set to 10^8 Nm/rad, and the gust gradient to H = 59 m. It should be noted that in this analysis, the flaps were deflected before the gust hits the wing and the loads are used where the gust velocity is assumed to result in an instantaneous change in the angle of attack.

4.1.1. Case 1: Inboard Flap Only

The inboard flap angle (β_1) is deflected in a step of 10° angle up and down for upward and downward gusts, respectively. The resulting gust response for different gust gradients is shown in Figures 12 and 13, respectively. It should be stressed that the deflections of the midboard and outboard flaps are set to zero.

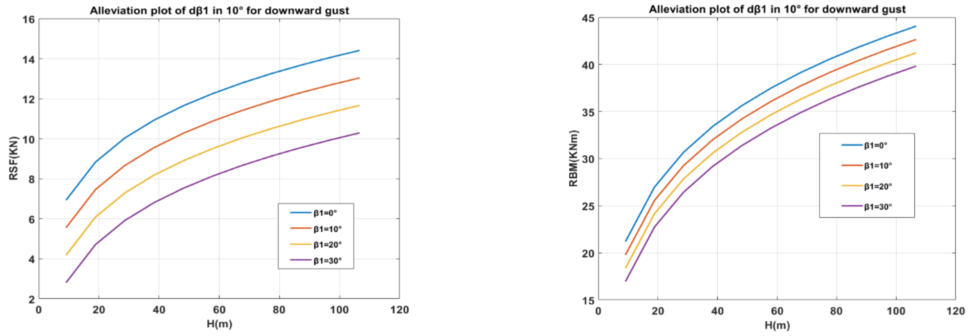

Figure 12. RSF and RBM at different gust gradients for downward gust.

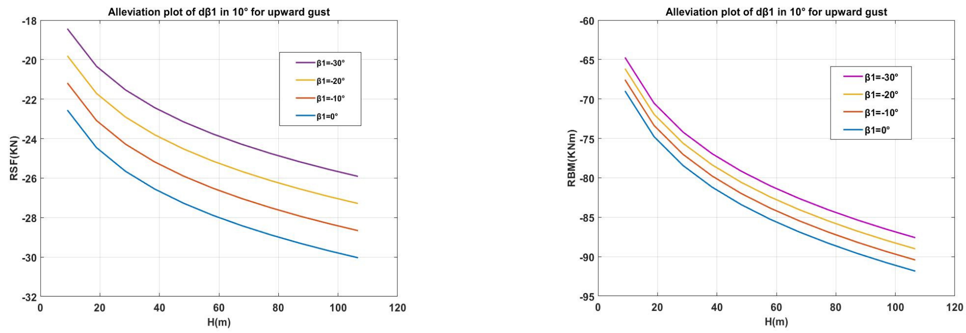

Figure 13. RSF and RBM at different gust gradients for upward gust.

Figure 12 (downward gust), when comparing with the baseline (blue) configuration, shows that RSF (8.14 kN) and RBM (33.24 kNm) are reduced by 33.63% and 11.32%, respectively, at a flap angle of 30° downward and H = 59 m. Increasing the flap deflection increases the alleviation percentage and at lower gust gradients a small deflection is enough to achieve more alleviation in RSF. From Figure 13 (upward gust), RSF (23.76 kN) and RBM (81.01 kNm) are reduced by 14.78% and 4.98%, respectively, for a flap angle of 30° upward and H = 59 m. Increasing the flap deflection increases the alleviation percentage.

4.1.2. Case 2: Midboard Flap Only

Similarly, the midboard flap angle (β_2) is deflected in a step of 10° angle up and down for upward and downward gusts, respectively. The resulting gust response for different gust gradients for downward and upward gusts are shown in Figures 14 and 15, respectively. It should be stressed that the deflections of the midboard and outboard flaps are set to zero.

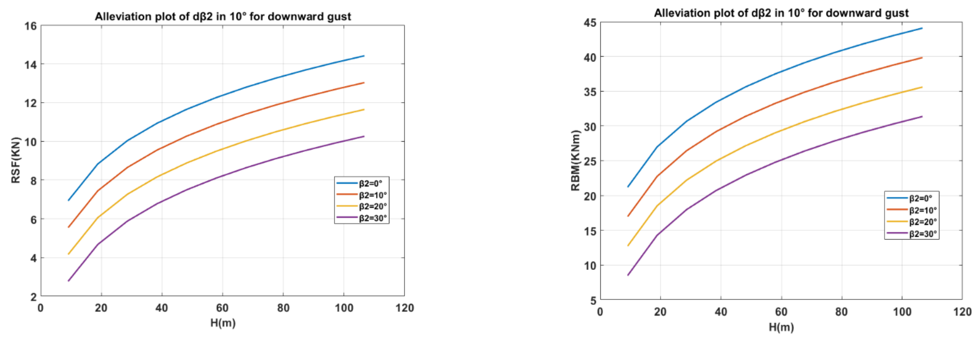

Figure 14. RSF and RBM at different gust gradients for downward gust.

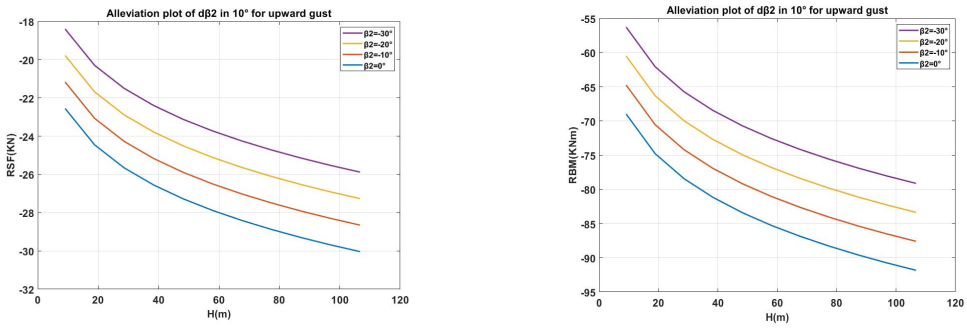

Figure 15. RSF and RBM at different gust gradients for upward gust.

Figure 14 (downward gust), when comparing with the baseline (blue) configuration, shows that RSF (8.10 kN) and RBM (24.77 kNm) are reduced by 33.91% and 33.92%, respectively, for a flap angle of 30° downward and H = 59 m. Increasing the flap deflection increases the alleviation percentage and a small deflection is enough to achieve more alleviation in both RSF and RBM. From Figure 15 (upward gust), RSF (23.73 kN) and RBM (72.55 kNm) are reduced by 14.90% and 14.91%, respectively, for a flap angle of 30° upward and H = 59 m. Increasing the flap deflection increases the alleviation percentage and both RSF and RBM vary gradually with flap deflection for all gust gradients.

4.1.3. Case 3: Outboard Flap Only

Only the outboard flap angle (β_3) is deflected in a step of 10° angle up and down for upward and downward gusts, respectively. The resulting gust responses for different gust gradients for downward and upward gusts are shown in Figures 16 and 17, respectively.

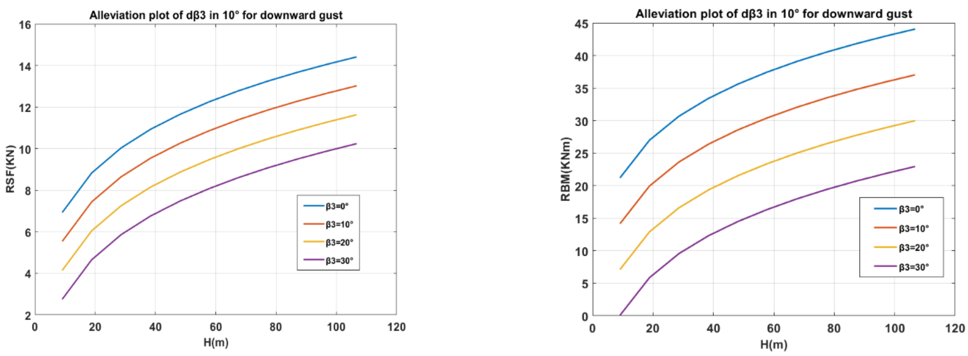

Figure 16. RSF and RBM at different gust gradients for downward gust.

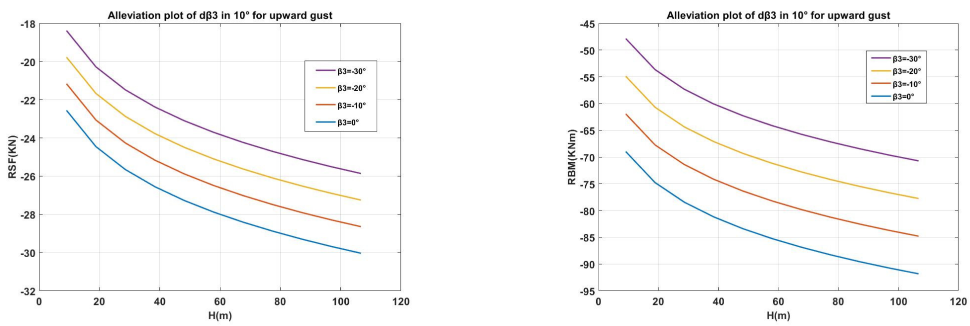

Figure 17. RSF and RBM at different gust gradients for upward gust.

Figure 16 (downward gust), when compared with baseline (blue), shows that RSF (8.08 kN) and RBM (16.35 kNm) are reduced by 34.07% and 56.37%, respectively, for a flap angle of 30° downward and H = 59 m. Increasing the flap deflection increases the alleviation percentage and a small deflection is enough to achieve more alleviation in both RSF and RBM. From Figure 17 (upward gust), RSF (23.71 kN) and RBM (64.13 kNm) are reduced by 14.97% and 24.91%, respectively, for a flap angle of 30° upward and H = 59 m. Increasing the flap deflection increases the alleviation percentage and both RSF and RBM vary gradually with flap deflection for all gust gradients.

From all the above cases, for downward gust, the RBM alleviation percentages are increasing from inboard to outboard but the RSF alleviation percentages are not showing any significant variation. For upward gust, both RSF and RBM alleviation percentages increase from inboard to outboard. It should be noted that the alleviation percentage is more in a downward gust as compared to an upward gust and this is because, for the downward gust, the downgoing flap will produce more aerodynamic opposing force than the upgoing flap as in the case of an upward gust. A more detailed summary of the response analysis is tabulated in Tables 3–6 for single-flap and multi-flap operations of SMTE.

Table 3. Summary of the percentage alleviation response of downward gust for different gust gradients.

Downward Gust	***H* = 9 m**		***H* = 59 m**		***H* = 106.7 m**	
	% Alleviation of RSF	**% Alleviation of RBM**	**% Alleviation of RSF**	**% Alleviation of RBM**	**% Alleviation of RSF**	**% Alleviation of RBM**
Inboard Flap only ($\beta_1 = 30^\circ$)	60	20	34	11	29	10
Midboard Flap only ($\beta_2 = 30^\circ$)	60	60	34	34	29	29
Outboard Flap only ($\beta_3 = 30^\circ$)	60	99	34	56	29	48

Table 4. Summary of the percentage alleviation response of upward gust for different gust gradients.

Upward Gust	***H* = 9 m**		***H* = 59 m**		***H* = 106.7 m**	
	% Alleviation of RSF	**% Alleviation of RBM**	**% Alleviation of RSF**	**% Alleviation of RBM**	**% Alleviation of RSF**	**% Alleviation of RBM**
Inboard Flap only ($\beta_1 = 30^\circ$)	18	6	15	4.9	14	4.6
Midboard Flap only ($\beta_2 = 30^\circ$)	18	18	15	15	14	14
Outboard Flap only ($\beta_3 = 30^\circ$)	18	31	15	25	14	23

Table 5. Summary of the percentage alleviation response of upward gust for a combination of flap deflections.

Upward Gust	***H* = 9 m**		***H* = 59 m**		***H* = 106.7 m**	
	% Alleviation of RSF	**% Alleviation of RBM**	**% Alleviation of RSF**	**% Alleviation of RBM**	**% Alleviation of RSF**	**% Alleviation of RBM**
Inboard and Midboard Flap ($\beta_1 = 30^\circ$)	37	25	30	20	28	18
Inboard and Outboard Flap ($\beta_2 = 30^\circ$)	37	37	30	30	28	28
Midboard and Outboard Flap ($\beta_3 = 30^\circ$)	37	49	15	40	14	37

Table 6. Comparison of percentage alleviation response for downward and upward gust.

	Downward Gust (H = 59 m)		Upward Gust (H = 59 m)	
	% Alleviation of RSF	% Alleviation of RBM	% Alleviation of RSF	% Alleviation of RBM
Inboard Flap only ($\beta_1 = 30°$)	34	11	15	5
Midboard Flap only ($\beta_2 = 30°$)	34	34	15	15
Outboard Flap only ($\beta_3 = 30°$)	34	56	15	25

4.2. Optimal Flap Deflections for Load Alleviation

In this work, optimal flap deflections are obtained for different load alleviation objectives and constraints. The inboard, midboard, and outboard flap angles (β_1, β_2 *and* β_3) are deflected in a step of 10° angle up and down for a downward gust. The gust (1-cosine) gradient is set at H = 9.07 m, while the airspeed is fixed to 30 m/s, the angle of attack is set to 0° and the flap stiffnesses are set to 10^8 Nm/rad. A set of 343 flap configurations are considered. For each configuration, the RSF, the RBM, and the percentage alleviation are computed. The results of the two different optimizations are reported as:

Objective 1: Minimize RBM subject to a 30% reduction in RSF: The objective is to find the optimal configuration that minimizes RBM and reduces the RSF by 30% relative to the baseline configuration (10,198 N) (flaps angles are zero).

Objective 2: Minimize RSF subject to a 30% reduction in RBM: The objective is to find the optimal configuration that minimizes RSF and reduces the RBM by 30% relative to the baseline configuration (31,084 N) (flaps angles are zero).

Table 7 presents the optimal configuration for each objective. In the case of Objective 1, the inboard and midboard flaps deflect to 30° while the outboard flap deflects to −28° giving a 66% reduction in RBM whilst reducing the RSF by 30%. However, for Objective 2, the midboard and outboard flap deflects to 30° while the inboard deflects to −4° resulting in a 52% reduction in RSF and a 30% reduction in RBM. To minimize RBM, the inboard flap deflects to the maximum angle while the midboard and outboard flaps deflect downward to the maximum angle. On the other hand, to minimize RSF, the inboard and midboard flaps deflect downward to the maximum angle whereas the outboard flap deflects slightly upward. It is worth noting that the ability to vary the spanwise camber distribution gives wider control on the RBM and RSF which is not the case with a single flap running from root to tip.

Table 7. Parameters of the selected configuration.

	Flap Angle (in Degrees)			RSF (in N)	RBM (in Nm)	% Alleviation of RSF	% Alleviation of RBM
	β_1	β_2	β_3				
Objective 1	−28	30	30	10,198	15,149	30	66
Objective 2	30	30	−4	7047	31,084	52	30

4.3. Comparison between a Single Flap and an SMTE (with Three Flaps)

The gust response of a single flap is obtained and presented in Table 8. The comparison is carried out in such a way that a single flap angle at 20° downward deflection can provide a 56% reduction in RSF and a 56% reduction in RBM. However, a 3-flap SMTE is capable of providing a 56% reduction in RBM with a 63% reduction in RSF. In addition, the SMTE is capable of providing a 56% reduction in RSF with a 78% reduction in RBM. Since SMTE allows spanwise camber variation, it gives the aircraft designer a wider range of options for load alleviation when compared to a single flap concept.

Table 8. Comparison between a single flap and an SMTE (with three flaps).

	Flap Angle (in Degrees)			RSF (in N)	RBM (in Nm)	% Alleviation of RSF	% Alleviation of RBM
Single Flap		β					
		20		6439	19,698	56	56
SMTE	β_1	β_2	β_3				
For the same RSF	10	30	30	439	98,344	56	78
For the same RBM	30	20	18	343	19,698	63	56

5. PID Controller for the SMTE Wing

Due to its simplicity and robustness, a PID controller is designed to meet the required loads at the wing root as shown in Figure 18. The PID controller delivers actuation force on SMTE to move from one position to another while maintaining the required load alleviation. The design of the PID controller did not account for actuator dynamics. To account for actuator dynamics, the type of actuation system must be determined and this requires trade-off studies that are beyond the scope of this paper which mainly aims to conduct a parametric aeroelastic study. The closed loop ensures that the achieved tip deflection is very close to the desired one. The controller parameters are proportional gain Kp, derivative gain Kd, and integral gain Ki. Percentage load alleviation was used to estimate control gains of the control system. There are many ways to tune a PID controller and there are also special methods for direct tuning based on simple process experiments. The PID tuning has been carried out based on the gust load alleviation values from the optimization study. A trial-and-error strategy was used to obtain the optimal control gain parameters.

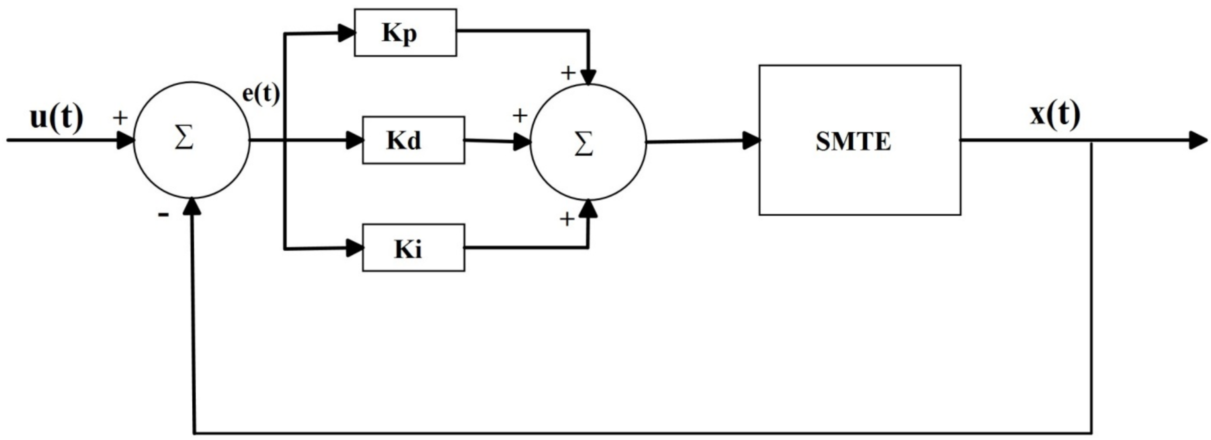

Figure 18. Block diagram of the PID controller.

This parametric study aims to have an initial investigation of a controller for SMTE. The gust alleviation property of SMTE was used to design controller parameters. If SMTE is used as a gust load alleviation device, it must be fast and must settle to the targeted wing root loads in the shortest period and with minimum overshoot. The selection of PID control gains is performed using the gust load alleviation values from the optimization study in Section 4.2. A trial-and-error strategy was used to reach control gain parameters. For a flight condition of 30 m/s, an angle of attack of zero radians, and at sea level, with a gust gradient of H = 9.07 m SMTE with three-flap configurations the controller parameters have been found out. Controllers with three different proportional gains, integral and differential gains have arrived at different combinations of flap angles. The simulations of the SMTE with three PID controllers were performed for different combinations of flap angles. For a given actuation time the integral gain is independent and a -1 (constant value) for differential gain gives minimum overshoot and stabilizes the system. Controller parameters for 30 percent load alleviation in root bending moment for some combinations of flap angles are tabulated in Table 9.

Table 9. Controller parameters**.**

Flap Angle (in Degrees)			Proportional Gain, Kp1	Proportional Gain, Kp2	Proportional Gain, Kp3	Differential Gain, Kd
β_1	β_2	β_3				
10	0	18	−5.89	0	−10.54	−1
10	10	12	−5.67	−5.67	−6.72	−1
10	20	6	−5.45	−10.90	−3.18	−1
10	30	0	−5.25	−15.76	0	−1
10	0	16	−11.41	0	−9.05	−1
10	10	10	−10.98	−5.49	−5.41	−1
10	20	2	−15.40	−10.27	−0.94	−1

6. Conclusions

This paper presented an investigation of the dynamic aeroelastic characteristics of a cantilever wing equipped with a spanwise morphing trailing edge (SMTE) concept. The structure of the wing was represented using the Euler–Bernoulli beam, the Rayleigh–Ritz method was used to derive the generalized equation of motion, and Theodorsen's unsteady aerodynamic theory was used to estimate the aerodynamic loads. The governing aeroelastic equations of the wing with a three-flap configuration were derived in the time domain. A flutter analysis was conducted to compute the flutter boundaries. The flutter boundaries of the wing with a three-flap configuration are compared with the wing with a single flap configuration. Furthermore, several scenarios were studied to assess the feasibility of SMTE as a load alleviation device when subject to discrete gusts. Finally, the implementation and validation of a controller for gust load alleviation were studied and controller parameters are tuned for a specific gust model. The simulation results showed the potential load alleviation capabilities of the SMTE when compared to a single flap configuration.

Author Contributions: Conceptualization, J.S.P. and R.M.A.; methodology, J.S.P. and R.M.A.; validation, J.S.P. and R.M.A.; formal analysis, J.S.P.; investigation, J.S.P. and R.M.A.; resources, R.M.A.; data curation, J.S.P.; writing—original draft preparation, J.S.P.; writing—review and editing, J.S.P., R.M.A., Z.H. and M.A.; supervision, R.M.A.; project administration, J.S.P. and R.M.A.; funding acquisition, R.M.A. All authors have read and agreed to the published version of the manuscript.

Funding: The work presented herein has been funded by the Abu Dhabi Education Council Award for Research Excellence Program (AARE 2019) through grant number AARE19-213.

Data Availability Statement: The data presented in this study are available on request from the corresponding author.

Conflicts of Interest: The authors declare no conflict of interest.

Nomenclature

a	non-dimensional distance from airfoil mid-chord to an elastic axis
b	airfoil semi-chord
$C(s)$	Theodorsen transfer function in the Laplace domain
c_i	non-dimensional distance from the airfoil mid-chord to the ith flap hinge line
L	Lift
M_α	moment of wing-flap about an elastic axis
$\mathrm{M}_{\beta\,\mathrm{i}}$	moment about the hinge axis of the ith flap
m	mass of wing-flap (per unit span)
y	spanwise location measured relative to the wing root

h	plunge displacement at the elastic axis
α	pitch angle
β_i	flap angle of the ith flap
V	true airspeed
$f(y)$	bending shape function
$\phi(y)$	torsion shape function
$\Psi(y)$	flap shape function
T	total kinetic energy
U	total potential energy
ρ	air density
S	Laplace variable
Acronyms	
Dof	degree of freedom
SMTE	spanwise morphing trailing edge
GLA	gust load alleviation
BWB	blended wing boy
PID	proportional integral derivative

Appendix A

It should be noted that the aeroelastic equation is of the general form $M\ddot{X} + D\dot{X} + KX$, where X is a vector of the system variables with an overdot representing time derivatives, the structural mass (M), and structural stiffness (K) matrices can be expressed as:

$$M = \begin{bmatrix} m & S_\alpha & S_{\beta_i} \\ S_\alpha & I_\alpha & \left(I_{\beta_i} + b(c_i - a)S_{\beta_i}\right) \\ S_{\beta_i} & \left(I_{\beta_i} + b(c_i - a)S_{\beta_i}\right) & I_{\beta_i} \end{bmatrix} \tag{A1}$$

$$K = \begin{bmatrix} K_h & 0 & 0 \\ 0 & K_\alpha & 0 \\ 0 & 0 & K_{\beta_i} \end{bmatrix} \tag{A2}$$

And

$$X = \begin{Bmatrix} h \\ \alpha \\ \beta_i \end{Bmatrix} \tag{A3}$$

References

1. Khalil, A.; Fezans, N. Performance Enhancement of Gust Load Alleviation Systems for Flexible Aircraft using H∞Optimal Control with Preview. In Proceedings of the AIAA Scitech 2019 Forum, San Diego, CA, USA, 7–11 January 2019. [CrossRef]
2. Bernhammer, L.O.; Navalkar, S.T.; Sodja, J.; De Breuker, R.; Karpel, M. Experimental investigation of an autonomous flap for load alleviation. In Proceedings of the 56th AIAA/ASCE/AHS/ASC Structures, Structural Dynamics, and Materials Conference, Kissimmee, FL, USA, 5–9 January 2015. [CrossRef]
3. Wildschek, A.; Stroscher, F.; Klimmek, T.; Šika, Z.; Vampola, T.; Valášek, M.; Gangsaas, D.; Aversa, N.; Berard, A.; Raumfahrt, L.U. Gust load alleviation on a large blended wing body airliner. In Proceedings of the 27th Congress of the International Council of the Aeronautical Sciences 2010, ICAS 2010, Nice, France, 19–24 September 2010.
4. Huvelin, F.; Dequand, S.; Lepage, A.; Liauzun, C. On the validation and use of high-fidelity numerical simulations for gust response analysis. *AerospaceLab J.* **2018**. [CrossRef]
5. Bekemeyer, P.; Thormann, R.; Timme, S. Investigation into gust load alleviation using computational fluid dynamics. In Proceedings of the International Forum on Aeroelasticity and Structural Dynamics 2019, IFASD 2019, Savannah, GA, USA, 10–13 June 2019.
6. Pusch, M. Allocation of distributed flaps for gust load alleviation. In Proceedings of the 1st Annual IEEE Conference on Control Technology and Applications, CCTA 2017, Kohala Coast, HI, USA, 27–30 August 2017; pp. 2120–2125. [CrossRef]
7. Dias, J.N.; Hubbard, J.J.E. *Active Spanwise Lift Control: A Distributed Parameter Approach*; American Institute of Aeronautics and Astronautics, Inc.: Reston, VA, USA, 2020. [CrossRef]
8. Pusch, M.; Knoblach, A.; Kier, T. Integrated optimization of control surface layout for gust load alleviation. *CEAS Aeronaut. J.* **2019**, *10*, 1059–1069. [CrossRef]

9. Barbarino, S.; Bilgen, O.; Ajaj, R.M.; Friswell, M.I.; Inman, D.J. A Review of Morphing Aircraft. *J. Intell. Mater. Syst. Struct.* **2011**, *22*, 823–877. [CrossRef]
10. Ajaj, R.M.; Parancheerivilakkathil, M.S.; Amoozgar, M.; Friswell, M.I.; Cantwell, W.J. Recent developments in the aeroelasticity of morphing aircraft. *Prog. Aerosp. Sci.* **2021**, *120*, 100682. [CrossRef]
11. Pankonien, A.M.; Inman, D.J. Spanwise morphing trailing edge on a finite wing. In *Active and Passive Smart Structures and Integrated Systems*; SPIE: San Diego, CA, USA, 2015; p. 94310T. [CrossRef]
12. Pankonien, A.M.; Inman, D.J. Aerodynamic performance of a spanwise morphing trailing edge concept. In Proceedings of the ICAST 2014—25th International Conference on Adaptive Structures and Technologies, The Hague, The Netherlands, 6–8 October 2014.
13. Haghighat, S.; Martins, J.R.R.A.; Liu, H.H.T. Aeroservoelastic Design Optimization of a Flexible Wing. *J. Aircr.* **2012**, *49*, 432–443. [CrossRef]
14. Capello, E.; Guglieri, G.; Quagliotti, F. A Comprehensive Robust Adaptive Controller for Gust Load Alleviation. *Sci. World J.* **2014**, *2014*, 1–12. [CrossRef] [PubMed]
15. Magar, K.T.; Fuchi, K.; Pankonien, A.M.; Beblo, R.V.; Reich, G.W. Active Control of Origami Inspired Camber Morphing Airfoil for Gust Load Alleviation. In Proceedings of the ASME 2018 Conference on Smart Materials, Adaptive Structures and Intelligent Systems, SMASIS, San Antonio, TX, USA, 10–12 September 2018. [CrossRef]
16. Bourchak, M.; Ajaj, R.M.; Flores, E.I.S.; Khalid, M.; Juhany, K.A. Optimum design of a PID controller for the adaptive torsion wing. *Aeronaut. J.* **2015**, *119*, 871–889. [CrossRef]
17. Kuznetsov, N.V.; Andrievsky, B.; Zaitceva, I.; Kudryashova, E.V.; Kuznetsova, O.A. Adaptive Suppression of Wing Flutter Under Actuator Saturation and Time Sampling. *IFAC-PapersOnLine* **2022**, *55*, 689–694. [CrossRef]
18. Mozaffari-Jovin, S.; Firouz-Abadi, R.; Roshanian, J. Flutter of wings involving a locally distributed flexible control surface. *J. Sound Vib.* **2015**, *357*, 377–408. [CrossRef]
19. Vindigni, C.R.; Orlando, C. Simple adaptive V-stack piezoelectric based airfoil flutter suppression system. *J. Vib. Control.* **2022**, *29*, 2802–2816. [CrossRef]
20. Muñoz, Á.; García-Fogeda, P. Active Flutter Suppression of a Wing Section in a Compressible Flow. *Aerospace* **2022**, *9*, 804. [CrossRef]
21. Wu, Z.; Lu, J.; Rajput, J.; Shi, J.; Ma, W. Adaptive Neural Control Based on High Order Integral Chained Differentiator for Morphing Aircraft. *Math. Probl. Eng.* **2015**, *2015*, 1–12. [CrossRef]
22. Seigler, T.M.; Neal, D.A.; Bae, J.-S.; Inman, D.J. Modeling and Flight Control of Large-Scale Morphing Aircraft. *J. Aircr.* **2007**, *44*, 1077–1087. [CrossRef]
23. Irani, S.; Sarrafzadeh, H.; Amoozgar, M.R. Bifurcation in a 3-DOF Airfoil with Cubic Structural Nonlinearity. *Chin. J. Aeronaut.* **2011**, *24*, 265–278. [CrossRef]
24. Chauhan, S.S.; Martins, J.R.R.A. Low-Fidelity Aerostructural Optimization of Aircraft Wings with a Simplified Wingbox Model Using OpenAeroStruct. In Proceedings of the EngOpt 2018 Proceedings of the 6th International Conference on Engineering Optimization, Libson, Portugal, 14 September 2018. [CrossRef]
25. Theodorsen, T. *General Theory of Aerodynamic Instability and the Mechanism of Flutter*; NACA Technical Report no.496; NASA: Washington, DC, USA, 1 January 1949; Volume 496.
26. Brunton, S.; Rowley, C. Low-Dimensional State-Space Representations for Classical Unsteady Aerodynamic Models. In Proceedings of the 49th AIAA Aerospace Sciences Meeting Including the New Horizons Forum and Aerospace Exposition, Orlando, FL, USA, 4–7 January 2011. [CrossRef]
27. Ajaj, R.M.; I Friswell, M. Aeroelasticity of compliant span morphing wings. *Smart Mater. Struct.* **2018**, *27*, 105052. [CrossRef]